Lifetimes and rotation within the solar mean magnetic field

Ross, Eddie; Chaplin, William J.; Hale, Steven J.; Howe, Rachel; Elsworth, Yvonne P.; Davies, Guy R.; Nielsen, Martin Bo

DOI:
10.1093/mnras/stab405

Monthly Notices
of the
ROYAL ASTRONOMICAL SOCIETY

MNRAS **502,** 5603–5611 (2021)
Advance Access publication 2021 February 11

doi:10.1093/mnras/stab405

Lifetimes and rotation within the solar mean magnetic field

Eddie Ross [1,2]★ William J. Chaplin,[1,2] Steven J. Hale,[1,2] Rachel Howe [1,2] Yvonne P. Elsworth,[1,2] Guy R. Davies[1,2] and Martin Bo Nielsen [1,2,3]

[1]*School of Physics and Astronomy, University of Birmingham, Edgbaston, Birmingham B15 2TT, UK*
[2]*Stellar Astrophysics Centre, Department of Physics and Astronomy, Aarhus University, Ny Munkegade 120, DK-8000 Aarhus C, Denmark*
[3]*Center for Space Science, NYUAD Institute, New York University Abu Dhabi, PO Box 129188, Abu Dhabi, United Arab Emirates*

Accepted 2021 February 8. Received 2021 February 5; in original form 2020 December 18

ABSTRACT

We have used very high-cadence (sub-minute) observations of the solar mean magnetic field (SMMF) from the Birmingham Solar Oscillations Network (BiSON) to investigate the morphology of the SMMF. The observations span a period from 1992 to 2012, and the high-cadence observations allowed the exploration of the power spectrum up to frequencies in the mHz range. The power spectrum contains several broad peaks from a rotationally modulated (RM) component, whose linewidths allowed us to measure, for the first time, the lifetime of the RM source. There is an additional broadband, background component in the power spectrum which we have shown is an artefact of power aliasing due to the low fill of the data. The sidereal rotation period of the RM component was measured as 25.23 ± 0.11 d and suggests that the signal is sensitive to a time-averaged latitude of $\sim 12^{\circ}$. We have also shown the RM lifetime to be 139.6 ± 18.5 d. This provides evidence to suggest that the RM component of the SMMF is connected to magnetic flux concentrations (MFCs) and active regions (ARs) of magnetic flux, based both on its lifetime and location on the solar disc.

Key words: Sun: activity – Sun: rotation .

1 INTRODUCTION

The Sun has a complicated magnetic field structure; many features of the Sun and proxies for the solar activity are related to the evolution of the Sun's magnetic field.

The solar mean magnetic field (SMMF) is a surprising, non-zero measurement of the imbalance of opposite polarities of magnetic flux observed on the full visible disc of the Sun (Svalgaard et al. 1975), and is defined as the mean line-of-sight (LOS) magnetic field when observing the Sun-as-a-star (Scherrer et al. 1977a,b; García et al. 1999). In the literature, the SMMF is also sometimes referred to as the general magnetic field (GMF; Severny 1971) or the mean magnetic field (MMF; Kotov 2008) of the Sun.

Observations of the SMMF have typically been made by measuring the Zeeman splitting of spectral lines using a ground-based Babcock-type magnetograph (Scherrer et al. 1977a), although more recently the SMMF has been calculated from full-disc LOS magnetograms taken from space-borne telescopes such as the Solar Dynamics Observatory/Helioseismic and Magnetic Imager (SDO/HMI; Kutsenko, Abramenko & Yurchyshyn 2017; Bose & Nagaraju 2018). It is understood that the strength of the SMMF may vary depending on the spectral line used to measure it (Kotov 2008, 2012); however, the SMMF varies slowly with the solar activity cycle, with an amplitude on the order of a Gauss during solar maximum and a tenth of a Gauss during solar minimum (Plachinda, Pankov & Baklanova 2011). In addition, the SMMF displays a strong, quasi-coherent rotational signal which must arise from inhomogeneities on the solar disc with lifetimes of several rotations (Chaplin et al. 2003; Xie, Shi & Xu 2017).

Despite existing literature on SMMF observations spanning several decades, the SMMF origin remains an open debate in solar physics. The principal component of the SMMF is commonly assumed to be weak, large-scale magnetic flux, distributed over the entire solar disc, rather than from magnetic flux concentrations (MFCs), active regions (ARs), or sunspots (Severny 1971; Scherrer et al. 1977a; Xiang & Qu 2016). However, conversely, Scherrer, Wilcox & Howard (1972) found that the SMMF was most highly correlated with only the innermost one quarter, by area, of the solar disc, which is more sensitive to active latitudes.

In recent literature, Bose & Nagaraju (2018) provided a novel approach to understanding the SMMF whereby they decomposed the SMMF through feature identification and pixel-by-pixel analysis of full-disc magnetograms. They concluded that: (i) the observed variability in the SMMF lies in the polarity imbalance of large-scale magnetic field structures on the visible surface of the Sun; (ii) the correlation between the flux from sunspots and the SMMF is statistically insignificant; and (iii) more critically that the background flux dominates the SMMF, accounting for around 89 per cent of the variation in the SMMF. However, there still remained a strong manifestation of the rotation signal in the background component presented by Bose & Nagaraju (2018). This signal is indicative of inhomogeneous magnetic features with lifetimes on the order of several solar rotations, rather than the

★ E-mail: exr007@student.bham.ac.uk

short-lived, weaker fields usually associated with the large-scale background. It therefore raises the question of whether their technique assigned flux from MFCs or ARs to the background. It is possible that some of the strong flux may have been assigned to the background signal, which then contributed to this rotation signal.

Despite these findings, it is known that the strength of the SMMF is weaker during solar minimum, when there are fewer ARs, and stronger during solar maximum, when there are more ARs (Plachinda et al. 2011). This is suggestive that the evolution of ARs has relevance for the evolution of the SMMF.

There is a contrasting view in the literature which claims AR flux dominates the SMMF. Kutsenko et al. (2017) state that a large component of the SMMF may be explained by strong and intermediate flux regions. These regions are associated with ARs, suggesting between 65 and 95 per cent of the SMMF could be attributed to strong and intermediate flux from ARs and the fraction of the occupied area varied between 2 and 6 per cent of the solar disc, depending on the chosen threshold for separating weak and strong flux. This finding suggests that strong, long-lived, inhomogeneous MFCs produce the strong rotation signal in the SMMF; however, Kutsenko et al. (2017) also discuss that there is an entanglement of strong flux (typically associated with ARs) and intermediate flux (typically associated with network fields and remains of decayed ARs). This means, it is difficult to determine whether strong ARs or their remnants contribute to the SMMF.

The Sun's dynamo and hence magnetic field is directly coupled to the solar rotation. The Sun exhibits latitude-dependent and depth-dependent differential rotation with a sidereal, equatorial period of around 25 d (Howe 2009). To Earth-based observers, the synodic rotation of the Sun is observed at around 27 days and the SMMF displays a dominant signal at this period, and its harmonics (Chaplin et al. 2003; Xie et al. 2017; Bose & Nagaraju 2018). It was also reported by Xie et al. (2017) that the differential solar rotation was observed in the SMMF with measured synodic rotational periods of 28.28 ± 0.67 and 27.32 ± 0.64 d for the rising and declining phases, respectively, of all of the solar cycles in their considered time-frame.

On the other hand, Xiang & Qu (2016) utilized ensemble empirical mode decomposition (EEMD) analysis to extract modes of the SMMF and found two rotation periods which are derived from different strengths of magnetic flux elements. They found that a rotation period of 26.6 d was related to weaker magnetic flux elements within the SMMF, while the measured period was slightly longer, at 28.5 d, for stronger magnetic flux elements.

In this work, we use high-cadence (sub-minute) observations of the SMMF, made by the Birmingham Solar Oscillations Network (BiSON; Chaplin et al. 1996, 2005; Hale et al. 2016), to investigate its morphology. This work provides a frequency domain analysis of the SMMF and a rotationally modulated (RM) component with a period of around 27 d is clearly observed as several peaks in the power spectrum. The breakdown of the paper is as follows.

In Section 2, we provide an overview of the BiSON data used in this work; how the observations are made and the SMMF data are acquired. As this work provides an investigation of the SMMF in the frequency domain, in Section 3, we discuss in detail how the power spectrum was modelled.

In Section 4, the results from modelling the power spectrum are presented. We outline the key findings and draw similarities between the properties of the RM component and ARs, suggesting that ARs may provide a strong contribution to the SMMF. Conclusions and discussions are presented in Section 5.

2 DATA

2.1 Summary of the data set

Chaplin et al. (2003) provided the first examination of the SMMF using data from the BiSON and the work presented in this paper is a continuation of that study.

BiSON is a six-station, ground-based, global network of telescopes continuously monitoring the Sun, which principally makes precise measurements of the line-of-sight (LOS) velocity of the photosphere due to solar p mode oscillations (Hale et al. 2016). Through the use of polarizing optics and additional electronics, the BiSON spectrometers can measure both the disc-averaged LOS velocity and magnetic field in the photosphere (Chaplin et al. 2003); however, not all BiSON sites measure the SMMF.

In this study, we focus on the data collected by the Sutherland node in South Africa, which was also used by Chaplin et al. (2003). This is the only station that has had the capability to measure and collect data on the SMMF long-term. Data are sampled on a 40-s cadence and the SMMF data collected by the Sutherland station span the epoch from 1992/01–2012/12 (i.e. covering 7643 d). Over this period, the average duty cycle of the 40-s data is ∼15.6 per cent. If instead we take a daily average of the BiSON SMMF, the average duty cycle is ∼55.2 per cent. This gives a higher duty cycle but a lower Nyquist frequency. Because of the much lower Nyquist frequency, modelling the background power spectral density is more challenging; therefore, we use the 40-s cadence data in this work. However, both data sets return similar results; we discuss later in Section 3.2 how we handled the impact of the low duty cycle of the 40-s data. A comparison of the daily-averaged SMMF observations made by BiSON to those made by the Wilcox Solar Observatory (WSO) is given in Chaplin et al. (2003).

2.2 Obtaining the SMMF from BiSON

To acquire the SMMF from BiSON data, the method described by Chaplin et al. (2003) was adopted; here, we discuss the key aspects.

Each BiSON site employs a resonant scattering spectrometer (RSS) to measure the Doppler shift of the Zeeman $^2S_{1/2} \rightarrow {}^2P_{1/2}$ line of potassium, at 769.9 nm (Brookes, Isaak & van der Raay 1978). A potassium vapour cell placed within a longitudinal magnetic field Zeeman splits the laboratory line into the two allowed D1 transitions (Lund et al. 2017). The intensity of the longer wavelength (red; I_R) and shorter wavelength (blue; I_B) components of the line may be measured by the RSS almost simultaneously, by using polarizing optics to switch between the red and blue wings of the line, to form the ratio given by equation (1) which is used as a proxy for the Doppler shift from the LOS velocity of the photosphere (see Brookes, Isaak & Raay 1976; Brookes et al. 1978; Elsworth et al. 1995a; Chaplin et al. 2003; Broomhall et al. 2009; Davies et al. 2014b; Lund et al. 2017)

$$\mathcal{R} = \frac{I_B - I_R}{I_B + I_R}. \tag{1}$$

Photospheric magnetic fields Zeeman split the Fraunhofer line and the Zeeman-split components have opposite senses of circular polarization (Chaplin et al. 2003). Additional polarizing optics are used in the RSS to manipulate the sense of circular polarization

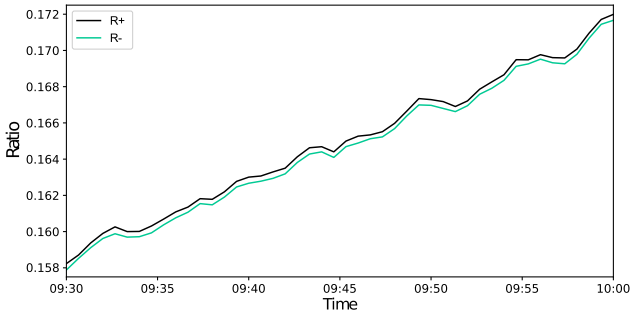

Figure 1. An example of the BiSON ratio data over a 30-min period. The separation between the two ratios is due to the SMMF and oscillations are due to the 5-min p mode signal.

(either + or -) that is passed through the instrument. The ratio $\mathcal{R}_+$ or $\mathcal{R}_-$ is formed, and the ratios $\mathcal{R}_\pm$ would be equal if there was no magnetic field present.

The observed ratio ($\mathcal{R}_\pm$) may be decomposed as

$$\mathcal{R}_\pm = \mathcal{R}_{\rm orb} + \mathcal{R}_{\rm spin} + \mathcal{R}_{\rm grs} + \delta r_{\rm osc}(t) \pm \delta r_{\rm B}(t), \tag{2}$$

where $\mathcal{R}_{\rm orb}$ is due to the radial component of the Earth's orbital velocity around the Sun, $\mathcal{R}_{\rm spin}$ is due to the component towards the Sun of the Earth's diurnal rotation about its spin axis as a function of latitude and time, $\mathcal{R}_{\rm grs}$ is from the gravitational red-shift of the solar line (Elsworth et al. 1995b; Dumbill 1999), $\delta r_{\rm osc}(t)$ is due to the LOS velocity due to p mode oscillations, and $\delta r_B(t)$ is due to the magnetic field ($\pm$ denotes the polarity of the Zeeman-split line that is being observed; Dumbill 1999). The effect of the magnetic field on the ratio is shown in Fig. 1 and from equation (3), the difference between the opposite magnetic field ratios is twice the magnetic ratio residual, i.e.

$$\mathcal{R}_+ - \mathcal{R}_- = 2\delta r_{\rm B}(t). \tag{3}$$

The BiSON RSS is measuring the velocity variation on the solar disc, and therefore a calibration from the ratio to a velocity is necessary. One method of calibration is achieved by first fitting a 2nd- or 3rd-order polynomial as a function of velocity to the observed ratio averaged over both magnetic polarities, as discussed by Elsworth et al. (1995b). Here, we chose to fit the ratio in terms of velocity, $\mathcal{R}_{\rm calc}(u)$, i.e.

$$\mathcal{R}_{\rm calc}(u) = \sum_n \mathcal{R}_n u^n, \tag{4}$$

where

$$u = v_{\rm orb} + v_{\rm spin}, \tag{5}$$

and $v_{\rm orb}$ is the velocity component related to the ratio, $\mathcal{R}_{\rm orb}$; $v_{\rm spin}$ is related to the ratio, $\mathcal{R}_{\rm spin}$; n is the polynomial order.

It is possible to see that through the removal of $\mathcal{R}_{\rm calc}(u)$ (which we set up to also account for $\mathcal{R}_{\rm grs}$) from the observed ratios, one is left with the ratio residuals of the p mode oscillations and the magnetic field, i.e.

$$\mathcal{R}_\pm - \mathcal{R}_{\rm calc}(u) = \delta r_{\rm osc}(t) \pm \delta r_{\rm B}(t). \tag{6}$$

Furthermore, conversion from ratio residuals into velocity residuals uses the calibration given by equation (7)

$$\delta v(t) = \left(\frac{{\rm d}\mathcal{R}_{\rm calc}}{{\rm d}V}\right)^{-1} \delta r(t). \tag{7}$$

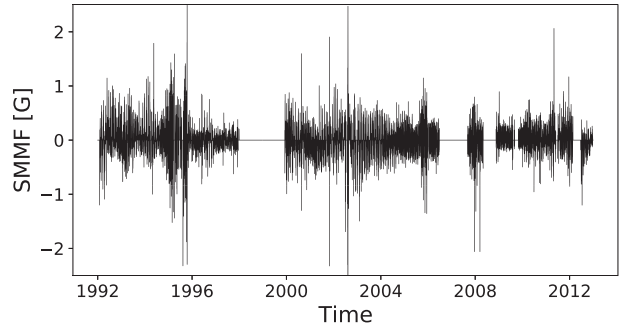

(a) Time-series of BiSON 40-s cadence SMMF

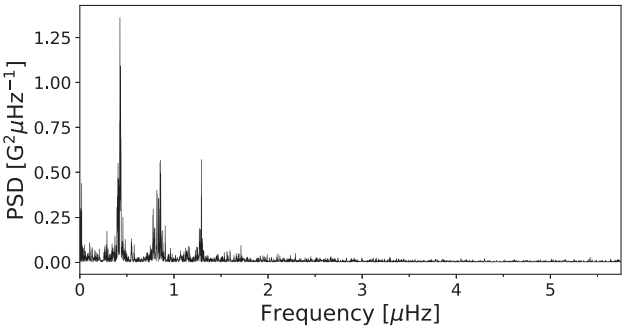

(b) Power spectrum of BiSON 40-s cadence SMMF

Figure 2. (a) 40-s cadence observations of the SMMF from the Sutherland BiSON station between 1992 and 2012. The sense of the field was chosen to match both Chaplin et al. (2003) and the WSO observations, where positive is for a field pointing outwards from the Sun. (b) Power spectrum of the SMMF on a 40-s cadence truncated to 10 μHz, however, the Nyquist frequency is 12 500 μHz.

In order to finally obtain the SMMF in units of magnetic field, one must combine equations (3) and (7) with the conversion factor in equation (9) (Dumbill 1999), and the entire procedure can be simplified into:

$$B(t) = \frac{1}{2}\left(\frac{d\mathcal{R}_{calc}}{dV}\right)^{-1} \frac{(\mathcal{R}_+ - \mathcal{R}_-)}{K_B}, \tag{8}$$

where

$$K_B = \frac{8}{3}\frac{\mu_B}{h}\frac{c}{\nu} \approx 2.89\,{\rm ms}^{-1}\,{\rm G}^{-1}, \tag{9}$$

and μ_B is the Bohr magneton, h is Planck's constant, c is the speed of light, and ν is the frequency of the photons.

Through the application of this methodology, one acquires the SMMF as shown in Fig. (2a). The power spectrum of the full, 7643-d Sutherland data set is shown in Fig. (2b), and it shows a strong rotational signal at a period of ∼27 d. The power spectrum of the SMMF is shown again in Fig. 3 on a logarithmic scale covering the entire frequency range, which highlights the broad-band background component of the power spectrum.

3 METHODOLOGY

3.1 Parametrization of the SMMF power spectrum

As we have 40-s cadence observations of the SMMF, we were able to investigate the power spectrum up to a Nyquist frequency of

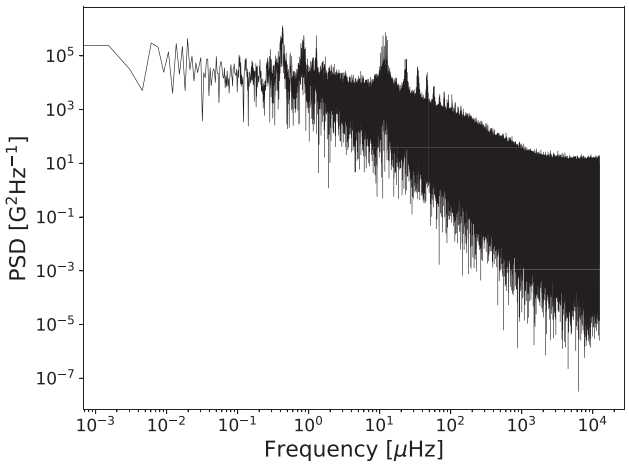

Figure 3. Power spectrum of 40-s cadence SMMF from the Sutherland BiSON station observed between 1992 and 2012 on a logarithmic scale up to the full Nyquist frequency.

12 500 μHz. There are a number of features within the full SMMF power spectrum, shown in Fig. 3.

The peaks between 0.2–2.0 μHz in Fig. 2(b) are a manifestation of rotation in the SMMF. The distinct set of peaks indicates the existence of a long-lived, inhomogeneous, RM source. Due to the quasi-coherent nature of the SMMF, and based on the comparatively short time-scales for the emergence of magnetic features compared to their slow decay (Zwaan 1981; Harvey & Zwaan 1993; Hathaway & Choudhary 2008), we assume the evolution of individual features that contribute to the RM component may be modelled by a sudden appearance and a long, exponential decay. In the frequency-domain, each of the RM peaks may therefore be described by a Lorentzian distribution

$$L_n(\nu;\Gamma,A_n,\nu_n)=\frac{2{A_n}^2}{\pi\Gamma}\left(1+\left(\frac{(\nu-\nu_n)}{\Gamma/2}\right)^2\right)^{-1}, \tag{10}$$

where ν is frequency, A_n is the root-mean-square amplitude of the peak, Γ is the linewidth of the peak, ν_n is the frequency of the peak, and n simply flags each peak. The mean-squared power in the time domain from the RM component of the SMMF is given by the sum of the ${A_n}^2$ of the individual harmonics in the power spectrum.

Through this formulation, we can measure the e-folding time (T_e) of the amplitude of the RM component, as it is related to the linewidth of the peak by

$$\Gamma=(\pi T_e)^{-1}. \tag{11}$$

The low-frequency power due to instrumental drifts, solar activity, and the window function can be incorporated into the model via the inclusion of a zero-frequency centred Lorentzian (Basu & Chaplin 2017), given by

$$H(\nu;\sigma,\tau)=\frac{4\sigma^2\tau}{1+(2\pi\nu\tau)^2}, \tag{12}$$

where σ is the characteristic amplitude of the low-frequency signal and τ describes the characteristic time-scale of the excursions around zero in the time-domain.

Finally, the high-frequency power is accounted for by the inclusion of a constant offset due to shot-noise, c (Basu & Chaplin 2017).

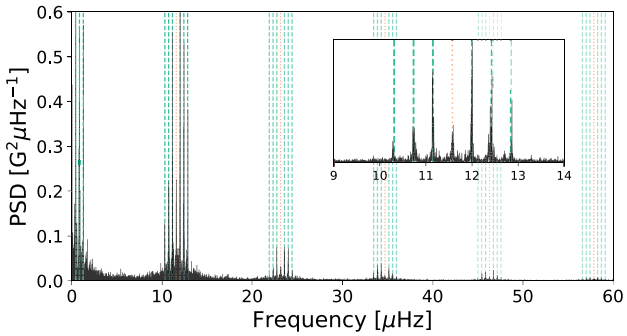

Figure 4. Locations of aliased power in sideband peaks. The orange dotted lines show the locations of frequencies at multiples of 1 per day. The green dashed lines show the location of the sideband peaks – harmonic frequencies reflected around multiples of 1 per day. The inset shows a zoom of one set of sideband peaks around 1 per day.

In the absence of any gaps in the data, the model function used to describe the power spectrum is given by

$$P(\nu,\boldsymbol{a})=\sum_{n=1}^{N}L_n(\nu;\Gamma,A_n,\nu_n)+H(\nu;\sigma,\tau)+c, \tag{13}$$

the subscript, n, describes a single peak in the power spectrum. In implementing the model, we constrain the mode frequencies such that they must be integer values of ν_0: $\nu_n=n\nu_0$. This means that we define a single rotation frequency only, ν_0, and subsequent peaks are the harmonic frequencies. It is worth noting explicitly that this function assumes the line width of each Lorentzian peak is the same, only the amplitudes and central frequencies differ.

The duty cycle of the Sutherland SMMF observations is very low, ∼15 per cent, therefore it was important to take into consideration the effect that gaps in the data have on the power spectrum. Gaps in the data cause an aliasing of power from the signal frequencies to other frequencies in the spectrum; and the nature of the aliasing depends on the properties of the window function of the observations.

Periodic gaps in the data give rise to sidebands in the power spectrum and random gaps cause a more broad-band shifting of power, meaning that some power from the low-frequency RM component is aliased to higher frequencies. The daily, periodic gaps in the BiSON data, due to single-site observations, produce sidebands around a frequency of 1 per day, i.e. ∼11.57 μHz, and its harmonics. The aliased power is therefore located at frequencies

$$\nu_{n,i}=i\left(\frac{1}{\text{day}}\pm\nu_n\right), \tag{14}$$

where i denotes the sideband number and n denotes the harmonic of the mode. The sideband structure implied by equation (14) is shown clearly in Fig. 4.

The tails of the aliased peaks are long, therefore aliased power was re-distributed across the entire frequency range which produced a red-noise-like background component. To understand the broad-band effects of the window function, we generated an artificial time series from a single Lorentzian (representing the fundamental RM component). The artificial data were generated by calculating the inverse Fourier transform of the power spectrum which had the same Nyquist frequency and frequency resolution of the SMMF power spectrum. We then injected the gaps from the BiSON observations into this artificial time series, to ensure the window function was the same as the BiSON SMMF, and finally investigated the resultant power spectrum both without and without the window function.

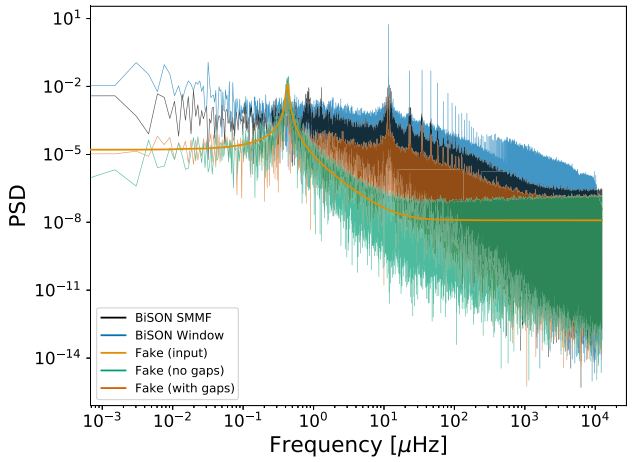

Figure 5. The effects of the window function on the power spectrum is shown by using a fake data set and this is compared to the BiSON power spectrum. Black line: BiSON SMMF power spectrum; blue line: power spectrum of the window function; green and dark-orange lines: the power spectrum of the artificial data without and with gaps, respectively; amber line: the input peak used to generate the artificial data overplotted. The power spectra of the BiSON SMMF and the window function have been shifted upwards by a factor of 6 and 30, respectively, for clarity.

Fig. 5 shows the effect of the window function on the resultant power spectrum. The power spectrum generated from the time series without gaps produces a single Lorentzian peak (amber and green lines). The injection of gaps into the time series (orange line) produces both the red-noise-like background component, as well as the sidebands, which bears a striking resemblance to the power spectrum of the BiSON SMMF observations (black line) and also the power spectrum of the window function (blue line).

This shows that the BiSON SMMF spectrum has a red-noise-like background component that is not due to any ephemeral signal, but due to the re-distribution of power by the window function of the BiSON observations.

In the time domain, the observed data, $y(t)$, includes the window function which, analytically, we can express as a multiplication of the uninterrupted, underlying signal, $f(t)$, with the window function, $g(t)$

$$y(t) = f(t)g(t), \tag{15}$$

where

$$g(t) = \begin{cases} 1 & \text{for } |B(t)| > 0 \\ 0 & \text{for } |B(t)| = 0 \end{cases}. \tag{16}$$

Multiplication in the time domain becomes a convolution in the frequency domain. To model the observed power spectrum in a robust manner, taking into account the intricacies caused by gaps in the data, we used a model which was formed of a model power spectrum, $P(\nu; \boldsymbol{a})$ (equation 13), convolved with the Fourier transform of the window function of the observations ($|\mathcal{F}[g(t)]|^2$), i.e.

$$P'(\nu, \boldsymbol{a}) = P(\nu, \boldsymbol{a}) * |\mathcal{F}[g(t)]|^2. \tag{17}$$

Care was taken during this operation to ensure Parseval's theorem was obeyed, that no power was lost or gained from the convolution

$$\sum_{\nu} P'(\nu) = \sum_{\nu} P(\nu) = \frac{1}{N} \sum_{t} B(t)^2, \tag{18}$$

where N is the number of observed cadences.

3.2 Modelling the SMMF power spectrum

Parameter estimation using the model defined in the previous section, including all parameters, $\boldsymbol{a}$, was performed in a Bayesian manner using a Markov chain Monte Carlo (MCMC) fitting routine.

Following from Bayes' theorem, we can state that the posterior probability distribution, $p(\boldsymbol{a}|D, I)$, is proportional to the likelihood function, $L(D|\boldsymbol{a}, I)$, multiplied by a prior probability distribution, $p(\boldsymbol{a}|I)$

$$p(\boldsymbol{a}|D, I) \propto L(D|\boldsymbol{a}, I)p(\boldsymbol{a}|I), \tag{19}$$

where D are the data and I is any prior information.

To perform the MCMC integration over the parameter space, we must define a likelihood function; however, in practice, it is more convenient to work with logarithmic probabilities. The noise in the power spectrum is distributed as χ^2 2 degrees of freedom (Anderson, Duvall & Jefferies 1990; Handberg & Campante 2011; Davies et al. 2014a), therefore the log likelihood function is

$$\ln(L) = -\sum_i \left\{ \ln(M_i(\boldsymbol{a})) + \frac{O_i}{M_i(\boldsymbol{a})} \right\}, \tag{20}$$

for a model, M_i, with parameters, $\boldsymbol{a}$, and observed power, O_i, where i describes the frequency bin. This likelihood function assumes that all the frequency bins are statistically independent but the effect of the window function means that they are not. We handled this issue in the manner described below, which used simulations based on the artificial data discussed in Section 3.1.

The prior information on each of the parameters used during the MCMC sampling were uniform distributions (denoted by $\mathcal{U}(l, u)$ with l and u representing the lower and upper limits of the distribution, respectively)

$$\begin{aligned}
\nu_0 &\sim \mathcal{U}(0.38, 0.50)\ \mu\text{Hz}, \\
\Gamma &\sim \mathcal{U}(0.00, 0.11)\ \mu\text{Hz}, \\
A_1 &\sim \mathcal{U}(100, 350)\ \text{mG}, \\
A_2 &\sim \mathcal{U}(50, 200)\ \text{mG}, \\
A_3 &\sim \mathcal{U}(20, 150)\ \text{mG}, \\
A_4 &\sim \mathcal{U}(10, 100)\ \text{mG}, \\
\sigma &\sim \mathcal{U}(0.01, 500)\ \text{mG}, \\
\tau &\sim \mathcal{U}(0.10, 200)\ 10^6\ \text{s}, \\
c &\sim \mathcal{U}(10^{-3}, 10^2)\ \text{G}^2\ \text{Hz}^{-1}.
\end{aligned}$$

The limits on the priors were set to cover a sensible range in parameter space, whilst limiting non-physical results or frequency aliasing.

The power spectrum of the 40-s cadence SMMF was modelled using equation (17) (with $N = 4$ Lorentzian peaks in $P(\nu, \boldsymbol{a})$) using the affine-invariant MCMC sampler EMCEE (Foreman-Mackey et al. 2013) to explore the posterior parameter space.

The chains are not independent when using EMCEE, therefore convergence was interrogated using the integrated autocorrelation time. We computed the autocorrelation time using EMCEE and found $\tau \sim 120$ steps. Foreman-Mackey et al. (2013) suggests that chains of length $\geq 50\,\tau$ are often sufficient. After a burn in of 6000 steps, we used 7000 iterations on 50 chains to explore the posterior parameter space, which was sufficient to ensure that we had convergence on the posterior probability distribution.

As a result of the convolution in the model, the widths of the posterior distributions for the model parameters were systematically underestimated. This effect arises because we do not account

Table 1. Power-spectrum model median results. Numbers in brackets denote uncertainties on the last two digits, and all uncertainties correspond to the 68per cent credible intervals either side of the median for adjusted posterior widths.

θ	Value	Unit	θ	Value	Unit
ν_0	$0.4270(^{+18}_{-18})$	μHz	A_4	32.6 ± 2.1	mG
Γ	$0.0264(^{+35}_{-35})$	μHz	τ	51.8 ± 6.8	days
A_1	166.0 ± 10.7	mG	σ	83.4 ± 5.4	mG
A_2	115.9 ± 7.4	mG	c	$0.2103\left(^{+03}_{-03}\right)$	G^2Hz^{-1}
A_3	83.2 ± 5.3	mG			

explicitly for the impact of the window function convolution on the covariance of the data; it is difficult to overcome computationally, especially with such a large data set ($\sim 10^7$ data points). To overcome this issue, we performed the simulations using artificial data, described above, both with and without the effects of the window function and the use of the convolution in the model. This helped us to understand how the convolution affected our ability to measure the true posterior widths, which allowed us to account for the systematic underestimate of the credible regions of the posterior when modelling the power spectrum of the observed BiSON SMMF.

We also analysed the data as daily, one-day-cadence averages; this gave a higher fill ($\sim$55 per cent) but a lower Nyquist frequency ($\sim$5.787 mHz). Because of the much lower Nyquist, modelling the background power spectral density was more challenging but the duty cycle was approximately three times higher, resulting in a smaller effect from the window function. We note that we recovered results in our analysis of the daily averaged data that were consistent with those from the analysis of the data with a 40-s cadence.

4 RESULTS

4.1 Rotation

From the adjusted posterior distributions for each of the parameters, acquired through modelling the power spectrum, we were able to measure the fundamental rotational frequency and linewidth of the RM component. The latter was assumed to be the same for each peak.

In Table 1, the median values of marginalized posterior distributions for each of the model parameters of equation (17) are displayed. The resultant posterior distributions were approximately normally distributed and there was no significant covariance between parameters, therefore reported uncertainties on the parameters correspond to the 68 per cent credible intervals either side of the median in the posterior distributions, adjusted for the systematic window function effects. In addition, we show the raw data with the model fit overplotted in Figs 6(a) and (b), on logarithmic and linear scales, respectively, to highlight the fit over the full frequency range, and the RM peaks, respectively.

The central frequency of the model, ν_0, implies a fundamental synodic rotation period of 27.11 $\pm$ 0.11 d, and hence a sidereal rotation period of 25.23 $\pm$ 0.11 d. The rotation period measured here is in agreement with other literature for the rotation signal in the SMMF (Chaplin et al. 2003; Xie et al. 2017).

According to the model for differential rotation in equation (A6), the measured rotation period suggests that the observed SMMF is sensitive to a time-averaged latitude of around 12°. This latitude is

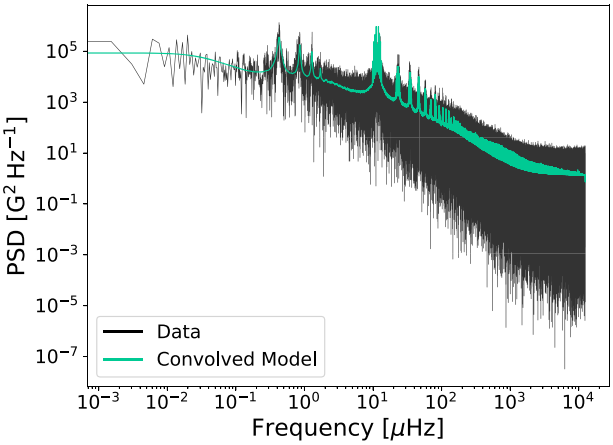

(a) Full power spectrum of the SMMF on logarithmic axes

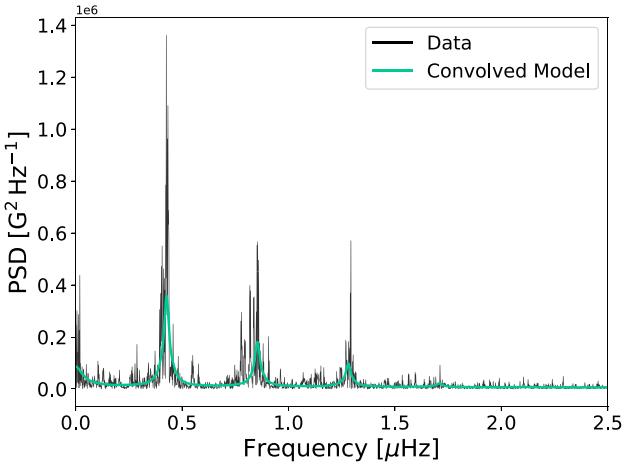

(b) Power spectrum of the SMMF on linear axes, up to a frequency of 2.5 μHz

Figure 6. Power spectrum and the best-fitting model for: (a) the full power spectrum of the SMMF on logarithmic axes. (b) Power spectrum of the SMMF on linear axes, up to a frequency of 2.5 μHz in order to show the fundamental signal peaks due to rotation-modulated ARs. The data is displayed in black and the model is shown in green.

consistent with those spanned by sunspots and ARs over the solar activity cycle (Maunder 1904; McIntosh et al. 2014), and particularly during the declining phase of the solar cycle (Thomas et al. 2019). This suggests the origin of the RM component of the SMMF could be linked to ARs.

4.2 Lifetimes

From the measured linewidth of the Lorentzian peaks, we have calculated the lifetime of the RM component using equation (11). The linewidth suggests a RM lifetime of 139.6 $\pm$ 18.5 d, which is in the region of $\sim$20 $\pm$ 3 weeks. The effects of differential rotation and AR migration do not impact our ability to measure the linewidth, and thus lifetime, of the peaks (as explained in Appendix A).

The typical lifetime of active magnetic regions and sunspots is on the order of weeks to months (Zwaan 1981; Howard 2001; Hathaway & Choudhary 2008), therefore, the observations of the SMMF by BiSON measure a lifetime of the RM component which is consistent with the lifetime of ARs and sunspots. This again suggests that the

RM signal is linked to ARs of magnetic field, suggesting them as a possible source of the signal.

When verifying these results by repeating the analysis with a daily averaged SMMF (see Section 3.2), the results for the linewidth were consistent.

5 DISCUSSIONS AND CONCLUSIONS

We have presented, for the first time, a frequency-domain analysis of ∼20 yr of high-cadence (40-s) BiSON observations of the SMMF.

The investigation of very high-cadence observations of the SMMF allowed the exploration of the power spectrum up to 12.5 mHz and the long duration of observations provided near-nHz resolution in the power spectrum which allowed us to measure the parameters associated with the RM component of the SMMF.

We have measured the central frequency of the RM component, allowing us to infer the sidereal period of the RM to be 25.23 ± 0.11 d. This rotation period matches to an activity cycle average latitude of ∼12°, which is in the region of the typical latitudes for active magnetic regions averaged over the activity cycle (Maunder 1904; McIntosh et al. 2014; Thomas et al. 2019).

For the first time, using the linewidth of the peaks, we have measured the lifetime of the RM component in the SMMF. The lifetime of the source of the RM component was inferred to be 139.6 ± 18.5 d. This lifetime is consistent with those of active magnetic regions and sunspots, in the region of weeks to months (Zwaan 1981; Hathaway & Choudhary 2008).

There has been considerable debate in the literature concerning the origin of the SMMF. In this study, as the properties of the RM component are consistent with ARs, we have presented novel evidence suggesting them as the source of the SMMF.

ACKNOWLEDGEMENTS

We would like to thank all those who are, or have been, associated with BiSON. The authors would like to acknowledge the support of the UK Science and Technology Facilities Council (STFC). Funding for the Stellar Astrophysics Centre (SAC) is provided by The Danish National Research Foundation (Grant DNRF106). This research also made use of the open-source PYTHON packages: ASTROPY,[2] a community-developed core PYTHON package for Astronomy (Robitaille et al. 2013; The Astropy Collaboration et al. 2018), CORNER (Foreman-Mackey 2016), EMCEE (Foreman-Mackey et al. 2013), MATPLOTLIB (Hunter 2007), NUMPY (Harris et al. 2020), PANDAS (McKinney 2010), and SCIPY (Virtanen et al. 2020).

DATA AVAILABILITY

This work uses data from the Birmingham Solar-Oscillations Network (BiSON), which may be accessed via the BiSON Open Data Portal.[1]

REFERENCES

Anderson E. R., Duvall T. L., Jr., Jefferies S. M., 1990, ApJ, 364, 699
Basu S., Chaplin W. J., 2017, Asteroseismic Data Analysis: Foundations and Techniques, Princeton Univ. Press, Princeton, NJ
Beck J. G., 2000, Sol. Phys., 191, 47
Bose S., Nagaraju K., 2018, ApJ, 862, 35
Brookes J. R., Isaak G. R., Raay H. B. v. d., 1976, Nature, 259, 92
Brookes J. R., Isaak G. R., van der Raay H. B., 1978, MNRAS, 185, 1
Broomhall A. M., Chaplin W. J., Elsworth Y., New R., 2009, MNRAS, 397, 793
Brown T. M., Christensen-Dalsgaard J., Dziembowski W. A., Goode P., Gough D. O., Morrow C. A., 1989, ApJ, 343, 526
Chaplin W. J. et al., 1996, Sol. Phys., 168, 1
Chaplin W. J., Dumbill A. M., Elsworth Y., Isaak G. R., McLeod C. P., Miller B. A., New R., Pintér B., 2003, MNRAS, 343, 813
Chaplin W. J., Elsworth Y., Isaak G. R., Miller B. A., New R., Pintér B., 2005, MNRAS, 359, 607
Chaplin W. J., Elsworth Y., New R., Toutain T., 2008, MNRAS, 384, 1668
The Astropy Collaboration et al., 2018, AJ, 156, 123
Davies G. R., Broomhall A. M., Chaplin W. J., Elsworth Y., Hale S. J., 2014a, MNRAS, 439, 2025
Davies G. R., Chaplin W. J., Elsworth Y., Hale S. J., 2014b, MNRAS, 441, 3009
Dumbill A. M., 1999, PhD thesis, School of Physics and Space Research, Univ. Birmingham
Elsworth Y., Howe R., Isaak G. R., McLeod C. P., Miller B. A., van der Raay H. B., Wheeler S. J., New R., 1995a, ASP Conf. Ser. Vol. 76, GONG '94: Helio- and Astero-Seismology from the Earth and Space, Astron. Soc. Pac., San Francisco, p. 392
Elsworth Y., Howe R., Isaak G. R., McLeod C. P., Miller B. A., New R., Wheeler S. J., 1995b, A&AS, 113, 379
Foreman-Mackey D., 2016, Corner.Py: Scatterplot Matrices in Python, http://joss.theoj.org
Foreman-Mackey D., Hogg D. W., Lang D., Goodman J., 2013, PASP, 125, 306
García R. A. et al., 1999, A&A, 346, 626
Hale S. J., Howe R., Chaplin W. J., Davies G. R., Elsworth Y. P., 2016, Sol. Phys., 291, 1
Handberg R., Campante T. L., 2011, A&A, 527, A56
Harris C. R. et al., 2020, Nature, 585, 357
Harvey K. L., Zwaan C., 1993, Sol. Phys., 148, 85
Hathaway D. H., Choudhary D. P., 2008, Sol. Phys., 250, 269
Howard R. F., 2001, The Encyclopedia of Astronomy and Astrophysics, IOP Publishing Ltd., Bristol
Howe R., 2009, Living Rev. Sol. Phys., 6
Hunter J. D., 2007, Comput. Sci. Eng., 9, 90
Jones E., Oliphant T., Peterson P., 2001, {SciPy}: Open Source Scientific Tools for {Python}, Vol 17, p. 261
Kotov V. A., 2008, Astron. Rep., 52, 419
Kotov V. A., 2012, Bull. Crimean Astrophys. Obs., 108, 20
Kutsenko A. S., Abramenko V. I., Yurchyshyn V. B., 2017, Sol Phys, 292, 121
Li K. J., Yun H. S., Gu X. M., 2001, AJ, 122, 2115
Lund M. N., Chaplin W. J., Hale S. J., Davies G. R., Elsworth Y. P., Howe R., 2017, MNRAS, 472, 3256
Maunder E. W., 1904, MNRAS, 64, 747
McIntosh S. W. et al., 2014, ApJ, 792, 12
McKinney W., 2010, in Proceedings of the 9th Python in Science Conference., Austin, TX, p. 51
Plachinda S., Pankov N., Baklanova D., 2011, Astron. Nachr., 332, 918
Robitaille T. P. et al., 2013, A&A, 558, A33
Scherrer P. H., Wilcox J. M., Howard R., 1972, Sol. Phys., 22, 418
Scherrer P. H., Wilcox J. M., Kotov V., Severnyj A. B., Severny A. B., Howard R., 1977a, Sol. Phys., 52, 3
Scherrer P. H., Wilcox J. M., Svalgaard L., Duvall T. L., Jr, Dittmer P. H., Gustafson E. K., 1977b, Sol. Phys., 54, 353
Severny A. B., 1971, Q. J. R. Astron. Soc., 12, 363
Snodgrass H. B., 1983, ApJ, 270, 288
Svalgaard L., Wilcox J. M., Scherrer P. H., Howard R., 1975, Sol Phys, 45, 83
Thomas A. E. L. et al., 2019, MNRAS, 485, 3857

[2] http://www.astropy.org
[1] http://bison.ph.bham.ac.uk/opendata

Virtanen et al. 2020 , Python. Nat Method, 261, 1548
Xiang N. B., Qu Z. N., 2016, AJ, 151, 76
Xie J. L., Shi X. J., Xu J. C., 2017, AJ, 153, 171
Zwaan C., 1981, NASA Special Publication, 450, 163

APPENDIX A: TESTING THE EFFECTS OF DIFFERENTIAL ROTATION AND MIGRATION

As a result of solar differential rotation and the migration of ARs towards the solar equator during the activity cycle, it is understood that the rotation period of ARs will vary throughout the solar cycle.

As we have inferred that the RM component of the SMMF is likely linked to ARs, we may therefore assume that the RM component is also sensitive to latitudinal migration. Here, we analysed the effect of this migration and differential rotation on our ability to make inferences on the lifetime of the RM component.

Several studies have modelled the the solar differential rotation and its variation with latitude and radius of the Sun (see Beck 2000 and Howe 2009 for in-depth reviews of the literature on solar differential rotation). Magnetic features have been shown to be sensitive to rotation deeper than the photosphere; therefore in general magnetic features can be seen to rotate with a shorter period than the surface plasma (Howe 2009).

Chaplin et al. (2008) analysed the effects of differential rotation on the shape of asteroseismic p modes of oscillation with a low angular degree (i.e. $l \leq 3$), and showed that the consequence of differential rotation is to broaden the observed linewidth of a mode peak. The authors provide a model of the resultant profile of a p mode whose frequency is shifted in time to be a time-average of several instantaneous Lorentzian profiles with central frequency $\nu(t)$, given by

$$\langle P(\nu)\rangle = \frac{1}{T}\int_0^T H\left(1+\left(\frac{\nu-\nu(t)}{\Gamma/2}\right)^2\right)^{-1} \mathrm{d}t\,, \tag{A1}$$

where the angled brackets indicate an average over time, H and Γ are the mode height (maximum power spectral density) and linewidth, respectively, and the full period of observation is given by T.

Chaplin et al. (2008) also show that by assuming a simple, linear variation of the unperturbed frequency, ν_0, from the start to the end of the time-series by a total frequency shift $\Delta\nu$

$$\nu(t) = \nu_0 + \Delta\nu\frac{t}{T}\,, \tag{A2}$$

the resultant profile of a p mode can analytically be modelled by equation (A3)

$$\langle P(\nu)\rangle = \frac{H}{2\epsilon}\arctan\left(\frac{2\epsilon}{1-\epsilon^2+X^2}\right)\,, \tag{A3}$$

where ϵ and X are defined in equations (A4) and (A5)

$$\epsilon = \frac{\Delta\nu}{\Gamma}\,; \tag{A4}$$

$$X = \frac{\nu-[\nu_0+(\Delta\nu/2)]}{\Gamma/2}\,. \tag{A5}$$

As the mode linewidths are broadened by this effect, we evaluated whether our ability to resolve the true linewidth of the RM, and hence the lifetime, was affected. In order to evaluate this, we computed the broadened profiles given by both equations (A1) and (A3), and fit the model for a single Lorentzian peak, to determine whether there was a notable difference in the linewidth.

In the first instance, we computed the broadened peak using equation (A1). Over the duration of the observations, we computed the daily instantaneous profile, $P(\nu(t))$. The time-averaged profile, $\langle P(\nu)\rangle$, was a weighted average of each instantaneous profile, where the weights were given by the squared-daily-SMMF, in order to allow a larger broadening contribution at times when the SMMF amplitude is higher.

In the second instance, we computed the broadened peak using equation (A3). Over the duration of the observations the daily frequency shift, $\Delta\nu$, was computed. The time-averaged shift, $\Delta\nu$, was a weighted average, where again the weightings were given by the squared-daily-SMMF.

To determine the shift in the rotation rate as the active bands migrate to the solar equator, we used the model of the solar differential rotation as traced by magnetic features (Ω_m) given by

$$\frac{\Omega_m}{2\pi} = 462 - 74\mu^2 - 53\mu^4\,\mathrm{nHz}\,, \tag{A6}$$

where $\mu = \cos\theta$ and θ is the co-latitude (Snodgrass 1983; Brown et al. 1989).

The time-dependence on the latitude of the ARs used the best-fitting quadratic model by Li, Yun & Gu (2001).

In both instances, the broadened peak was modelled as a single Lorentzian peak using equation (10). Again, we use EMCEE (Foreman-Mackey et al. 2013) to explore the posterior parameter space, with priors similar to the above full-fit on the relevant parameters.

A1 Results: Time-averaged broadened profile

Over the entire duration of the SMMF observations, the time-averaged profile was calculated, using equation (A1), and this is shown in Fig. A1a. The broadened mode used the input parameters outlined in Table 1, however with the background parameter set to zero.

By eye, the broadened profile does not appear to have a significantly larger linewidth. The input linewidth was $0.0264 \pm 0.0035\,\mu$Hz, and the fit to the time-averaged broadened peak produced a linewidth of $0.0262^{+0.0038}_{-0.0037}\,\mu$Hz. The linewidth of the broadened peak under this method was rather unchanged from that of the true peak, and both linewidths are within uncertainties of each other.

This result shows that numerically, the mode broadening effect of differential rotation and migration does not affect our ability to resolve the linewidth of the peak, and hence the predicted lifetime of the RM component of the SMMF.

A2 Results: Analytically Broadened Profile

The time-averaged frequency shift due to differential rotation was calculated, much in the same way as equation (A1), to be $\Delta\nu = 0.01285\,\mu$Hz. This shift was used to generate the broadened profile using equation (A3). The broadened mode distribution also used the input parameters outlined in Table 1, however, with the background parameter set to zero.

Similar to the numerically broadened peak, by eye, the analytically broadened profile does not appear to have a significantly larger linewidth (see Fig. A1b). The input linewidth was $0.0264 \pm 0.0035\,\mu$Hz, and the linewidth of the analytically broadened peak from the fit was $0.0263^{+0.0038}_{-0.0037}\,\mu$Hz, which was within the uncertainties of the linewidth of the input peak.

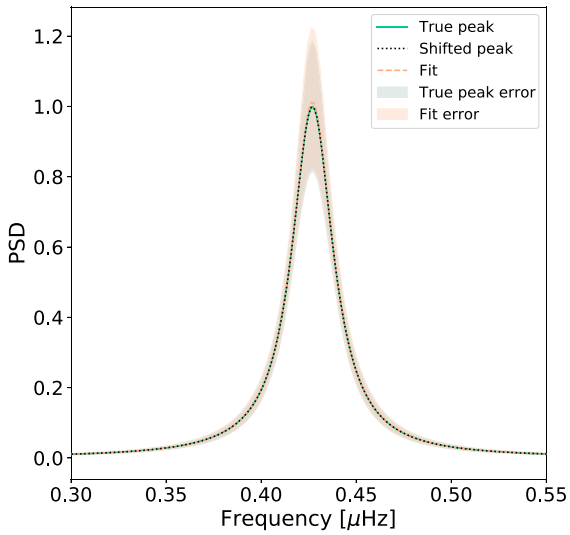

(a) Time-Averaged Broadened Profile

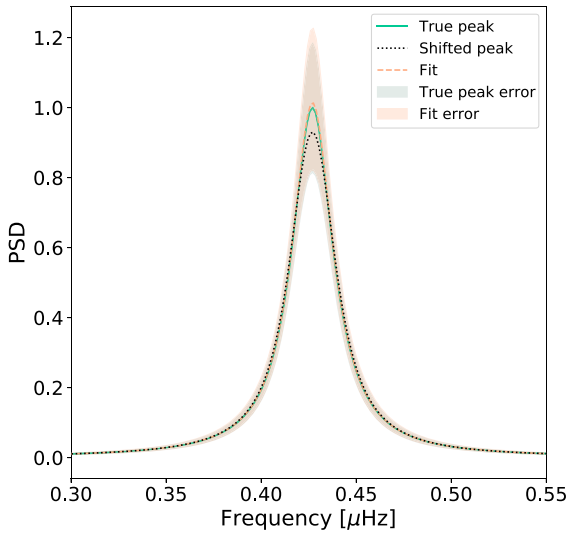

(b) Analytically Broadened Profile

Figure A1. Panel (a) shows the peak distribution before and after the time-averaged broadening, and the fit to the broadened peak. Panel (b) shows the peak distribution before and after the analytical broadening, and the fit to the broadened peak. In both plots, the broadened peaks have been shifted by the relevant frequency to overlay them on top of the true ν_0 for comparison.

This result shows, analytically, the mode broadening effect of differential rotation and migration does not affect our ability to resolve the linewidth of the peak, and hence the lifetime of the RM component of the SMMF.

A3 Discussion

Both broadening methods applied were shown to have a negligible effect on the linewidth of the profile, and our ability to resolve the true linewidth of the peak remains unaffected. This result provides confidence that the measured linewidth in Table 1 was the true linewidth of the RM peaks, providing the correct lifetime for RM component, unaffected by migration and differential rotation.

This paper has been typeset from a TEX/LATEX file prepared by the author.